JOURNAL OF SOLID STATE CHEMISTRY 92, 543–564 (1991)

Microdomains in Urania-Yttria and Urania-Ceria

M. C. PIENKOWSKI,* M. L. JENKINS, AND P. T. MOSELEY†

Department of Materials, University of Oxford, Parks Road, Oxford, OX1 3PH, United Kingdom; and †Materials Development Division, Harwell Laboratory, Didcot, Oxon, OX11 ORA, United Kingdom

Received June 4, 1990; in revised form December 21, 1990

The mixed uranium oxides $(U_{0.4}, Y_{0.6})O_{2\pm x}$ and $(U_{1-y}, Ce_y)O_{2\pm x}$, where $y = 0.2, 0.4, 0.6$ have been studied using selected-area electron diffraction (SAD) and high-resolution electron microscopy (HREM). Electron diffraction patterns from cubic solid solutions of urania-yttria contained diffuse features in addition to the strong reflections expected from the fluorite structure type. These SAD observations were consistent with HREM experiments which showed subtle modulations of contrast in the matrix planes. It is suggested that these diffuse features arise from small domains of size ~30 Å embedded coherently in a number of orientations within the cubic matrix. Although there were some similarities between the diffuse scattering observed in this material and that observed for the case of yttria-doped zirconia, attempts to identify the structures of the microdomains explicitly were unsuccessful. Ordered domains have also been seen in $(U_{1-y},Ce_y)O_{2\pm x}$ solid solutions, having values of $y = 0.4$ and 0.6, using the technique of lattice imaging. It is concluded that these domains are likely to have adopted a partially ordered pyrochlore structure. In contrast, single crystals of urania-ceria having a ceria content of $y = 0.2$ showed no evidence of cation ordering. Instead, the most common features observed were dislocations having a Burgers vector consistent with the type $\frac{1}{2}\langle 110\rangle_f$ in projection.

1. Introduction

Urania-yttria and urania-ceria solid solutions are of interest because they are useful as components for high-temperature fuel cells and as simulants for nuclear fuel, respectively. These solid solutions are known to have fluorite-type structures over a wide range of composition. They are stable in reducing atmospheres such as carbon monoxide and hydrogen. Reduction changes the oxidation state of uranium and the overall oxygen–metal ratio but does not destroy the basic structural integrity of the material. A recent report in this journal (*1*) has described the use of electron diffuse scattering to provide evidence of microdomains in the system U–La–O. The present work describes a study into the manner in which stoichiometric variability is accommodated in fluorite-related structures adopted by the related systems U–Y–O and U–Ce–O.

The detailed microstructures of these materials have not been studied in great detail, but it is known that under certain conditions materials with the fluorite structure, including urania-yttria solid solutions, may transform entirely or partially into a number of fluorite-related phases. Solid solutions of

* To whom correspondence should be addressed at present address: Department of Chemistry, Heriot-Watt University, Edinburgh, EH14 4AS, Scotland.

0022-4596/91 $3.00

UO_{2+x} and Y_2O_3 and mixtures of UO_{2+x} with RE_2O_3 (where RE = Ho, Tm, and Lu) (*2*) and solid solutions of rare-earth metal oxides and transition metal oxides (*3*) have long been known to form the fluorite structure with a degree of anion deficiency which depends upon the rare-earth metal ion content and the oxygen partial pressure. When the number of oxygen vacancies becomes too large, a structural rearrangement takes place to give a family of cells having the rhombohedral structure designated RhI applied to the general formula $U_pY_{7-p}O_{12}$ where $2 > p > 1$. In the case of urania-yttria solid solution, when oxidized above 1000°C, the limiting composition at which this is reported to occur is at an yttria content of 50 mole% (*4*). The lattice parameters of this phase range from a = 6.580 Å and α = 99.356° when the composition is $17UO_{2.17} \cdot 18Y_2O_3$ to a = 6.530 Å and α = 99.05 when the composition is $UO_3 \cdot 3Y_2O_3$ and the phase has space group $R\bar{3}$ (No. 148). The phase $U_2Y_5O_{13.3}$ (sometimes referred to as RhII in the literature), with an O/U ratio of 2.9 and lattice parameters a = 6.522 Å and α = 99.05°, may be formed by a low temperature (below 1000°C) oxidation of $U_2Y_5O_{12}$. Four extra oxygen ions can be taken into the hexagonal cell ($\frac{4}{3}$ into trigonal cell). These additional oxygen ions are statistically distributed in the 6(c) special positions (2(c) trigonal cell) of $R\bar{3}$.

The work on the UO_2–UO_3–Y_2O_3 system outlined above concentrated on phases in the oxygen-poor, yttrium-rich region and very little work has been done on soild solutions with high O/U ratios: Indeed, none at all has been done in the region of interest here (namely Y_2O_3 content of 43% and an approximate O/U ratio of 3). Bartram and Fitzsimmons reported the observation of an ordered oxide phase of composition UYO_4 in which the O/U ratio was 2.50, in a solid solution of UO_2–10 wt%Y_2O_3 (~12 mole%Y_2O_3) (*5*) having lattice parameters a = 5.519 Å, b = 5.632 Å, c = 5.252 Å. The phase has orthorhombic centrosymmetric space group *Bmmm* (No. 65) with systematic absences $h + l \neq 2n$. Ainscough and Ferguson conducted oxidation studies on a series of urania-yttria solid solutions that had oxygen : uranium ratios greater than 2.667 and yttria contents in the range 0–10 mole% (*6*). These oxidized materials all consisted of a single α-U_3O_8-like orthorhombic phase, the symmetry of which changed from orthorhombic to orthorhombic–pseudohexagonal as more yttria was dissolved in it, thus approaching the symmetry of β-U_3O_8, the closely related high temperature hexagonal polymorph of α-U_3O_8.

Investigations of the UO_2–CeO_2–U_3O_8 system (*7*), using X-ray powder diffraction, have revealed that, in general, reduction of the mixed oxide to a hypostoichiometric composition results in the formation of two phases, MO_2 and MO_{2-x} in equilibrium at room temperature. This is in contrast to urania-yttria which is capable of forming well-ordered phases.

Electron microscopy and electron diffraction have been used to study the zirconium-based system but prior to the present study no comparable information has been published on the uranium-based system. The purpose of this work was to consolidate previous knowledge of these systems with results obtained from electron microscopy. Diffuse features seen in urania-yttria and urania-ceria first reported by the authors (*8*) were found to be similar in some respects to the diffuse features described found for stabilized zirconia (*9*) and hafnia (*10*) systems and attributed to microdomains of a fluorite-related phase designated ϕ_1. Our observations in urania-yttria and urania-ceria are described below.

2. Experimental

The electrode material urania-yttria was kindly supplied by Dr. Badwal of the Materials Science and Technology Division of

CSIRO in Victoria, Australia. It had composition $(U_{0.4}, Y_{0.6})O_{2\pm x}$ and had been prepared in the following manner (*11*): First a nitric acid solution containing the desired amounts of Y_2O_3 and U_3O_8 necessary to form $(U_{0.4}, Y_{0.6})O_{2\pm x}$ was prepared. Then the metal hydroxide was coprecipitated by adding excess ammonia solution. The precipitate was washed, dried, and calcined at 700°C for 15 hr in air so as to drive off any volatile impurities. All the starting materials had 99.97% purity. In this work the oxygen–metal ratio, $O/M = 2 \pm x$, has not been determined. However, in air it has been shown (*12*) that the O/M values for $(U_{0.45}, Y_{0.55})O_{2\pm x}$ and $(U_{0.4}, Y_{0.6})O_{2\pm x}$ are close to 2.0 at 1300°C.

The method of urania-ceria sample preparation was similar to the method used in the manufacture of fuel rods (*13*). Weighed amounts of stoichiometric uranium dioxide and cerium dioxide powders were blended and then pressed using a die to form pellets having dimensions 16 mm × 10 mm. Three different compositions of $(U_{1-y}, Ce_y)O_{2\pm x}$ having values of $y = 0.2$, 0.4, and 0.6 were prepared. These were then fired at 1600°C under an atmosphere of CO/CO_2 for 3 days. After annealing, the pellets were ground and pressed for a second time and the heat treatment was repeated. This was done to ensure the homogeneity of cations in the sample while ensuring that the material remained stoichiometric. Finally the pellets were ground to a fine powder and reduced under flowing hydrogen gas at 1400°C using a Metals Research PCA10 tube furnace within an argon-filled glovebox. Again the O/M ratio was not measured in this work but a limit can be put on its value. A lower limit on x is achieved when the Ce^{4+} ions are all reduced to Ce^{3+}, where in order to preserve electrical neutrality $x = \frac{y}{2}$.

Some of the mixed oxides received further heat treatments. This was done for two reasons: First, there was a problem preparing the as-received electrode material for TEM work. Upon crushing urania-yttria powders, particles (of size ~500 nm) tended to form large agglomerate masses that were opaque to electrons. Attempts were made to disperse these particles using commercial deflocculating agents but these attempts were unsuccessful. Annealing at 1600°C proved effective in increasing the grain size, thus inhibiting particle agglomeration. Second, ageing also enhanced atomic ordering. High temperatures and long anneal times were necessary because of the low values of metal ion mobilities. In uranium dioxide, for example, the diffusion coefficient for uranium ions is $\sim 10^{-17}$ cm^2s^{-1} at a temperature of 1400°C, a factor of $\sim 10^5$ smaller than the oxygen mobility (*14*). Because of their low mobilities, the diffusion of cations is a rate determining step for many high temperature processes.

Specimens for electron microscopy were prepared by crushing the powders in an agate mortar under ethanol. Small particles were then scooped up onto perforated carbon films supported on 400 mesh 3.05-mm diameter copper grids. Selected-area diffraction and high-resolution imaging experiments were performed on a JEOL 4000EX electron microscope with a point to point resolution of 1.6 Å and $C_s = 1$ mm. These grids had their bars annotated so that small crystallites could be easily found for later microanalysis in a Philips CM12 microscope.

3. Observations of Microdomains in Urania-Yttria

3.1. X-Ray Diffraction Observations

X-ray diffractograms were obtained using a Siemens D500 diffractometer at Harwell set up for the Hull (*15*) Debye–Scherrer (*16*) technique and lattice parameters were determined using the Cohen method of least squares (*17*).

The lattice parameter of the "as supplied" green–black sample was calculated to be 5.332(1) Å. Upon ageing at 1000°C, urania-yttria showed a contraction in the fluorite lattice parameter of ~0.5%. The fluorite lattice parameter was 5.3268(2) Å for the furnace-cooled sample. Diffractograms from neither of these samples exhibited any features between the Bragg peaks, showing that in these cases the solid solution remains within the fluorite phase field. Annealing of urania-yttria at 1600°C resulted in a larger contraction of the unit cell of ~2% to produce a cell having lattice parameter 5.313(1) Å. The color of the heat-treated powder was yellow and the diffractogram indicated a strong splitting of the $\{111\}_f$ Bragg peak with weaker peaks occurring at lower Bragg angles (see Fig. 1). The compositions of small crystallites of this material were found by energy-dispersive X-ray microanalysis to be within 20% of the bulk composition. However, a small proportion were found to be devoid of uranium and these were found to have the *C*-type rare earth structure (*18*).

3.2. Electron Diffraction Observations

Only the sample which had been annealed for 3 days at 1600°C was examined by electron microscopy since the samples annealed at lower temperatures showed no evidence in X-ray diffraction of phase separation. Selected-area diffraction patterns were obtained from several crystals of various orientations and from each crystal several poles were recorded by sweeping along Kikuchi bands in the reciprocal space triangle having apex poles $\langle 001\rangle_f$, $\langle 111\rangle_f$, and $\langle 011\rangle_f$.

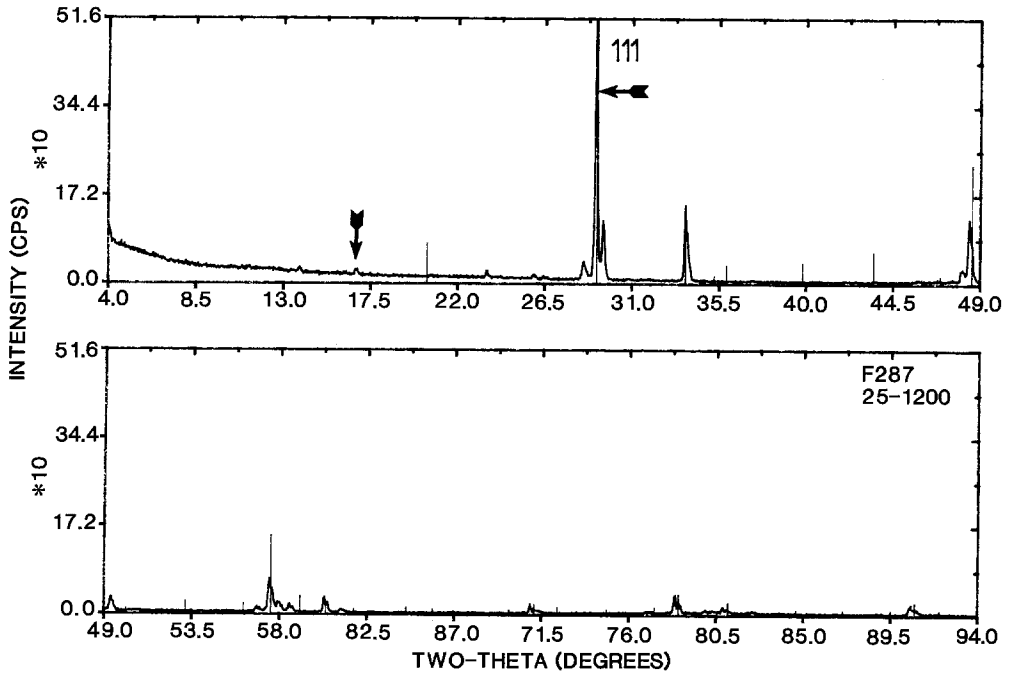

FIG. 1. X-ray powder diffraction of urania-43% yttria furnace cooled from 1600°C (a_f = 5.313(1) Å). The $\{111\}_f$ Bragg peak is split and weaker nonfluorite peaks can be seen at small values of $2\theta_B$ (one such peak is arrowed). The spikes mark the literature values of the positions of Bragg reflections from yttrium sesquioxide which crystallizes in the *C*-type rare-earth structure (lattice parameter 9.845 Å).

The zone axes scanned in total were $\langle 001\rangle_f$, $\langle 116\rangle_f$, $\langle 114\rangle_f$, $\langle 112\rangle_f$, $\langle 111\rangle_f$ on the $2\bar{2}0$ band and the poles $\langle 233\rangle_f$, $\langle 122\rangle_f$, $\langle 011\rangle_f$ located on the $0\bar{2}2$ band at 60° to it. In addition the zone axes $\langle 125\rangle_f$ and $\langle 013\rangle_f$ were examined by tilting respectively along the $3\bar{1}1$ and $13\bar{1}$ bands from the $\langle 114\rangle_f$ pole and the $\langle 012\rangle_f$ zone axis by tilting along the 200 band from $\langle 013\rangle_f$. Representative results of patterns obtained at some of these poles are shown in Figs. 2a–2e.

It can be seen that in addition to reflections that are expected for a face-centered cubic real space lattice, each zone axis exhibits diffuse electron scattering between the nodes of the mean fluorite Bragg reflections. The overall appearance of the patterns is also shown schematically in the diagrams accompanying the electron diffraction patterns (Fig. 2), where for clarity the fluorite reflections are represented by an array of black circles and the diffuse intensity maxima are represented by smaller black dots. These maxima may be connected by fainter diffuse features which are adumbrated. The intensity of the diffuse scattering can be seen to be stronger at some poles than at others.

3.3. Geometry of the Diffuse Scattering

The diffuse intensity appears weakest and of a lower density in zone axes $\langle 001\rangle_f$ and $\langle 111\rangle_f$ located on two of the vertices of the stereographic triangle. At the third vertex, the $\langle 110\rangle_f$ pole, however, the extra reflections are strong. High order zones generally have a higher density of diffuse intensity and some of them exhibit distinct diffuse annuli. This is particularly apparent at the $\langle 112\rangle_f$ and $\langle 233\rangle_f$ zone axes (Figs. 2c and 2d, respectively). In the $\langle 112\rangle_f$ pattern the "smoke-rings" are located at centroids of the rectangles formed by the fundamental Bragg beams ($\frac{1}{2}(2n + 1)\langle 131\rangle^*_f$ positions, where n is an integer) and are quasicircular. In the $\langle 233\rangle_f$ pole, the diffuse features are located at $\frac{1}{2}(2m + 1)\langle 131\rangle^*_f + n\langle 220\rangle^*_f$ positions (where m and n are both integers) and are quasi-square.

From this series of zone axis patterns, the three-dimensional geometry of the diffuse scattering intensity can be deduced. The reciprocal lattice of the real-space face-centered lattice is a body-centered cubic cell containing two reciprocal lattice points and it is invariant to the symmetry operations of the space group $Im3m$. The diffuse intensity also exhibits the same symmetry and occupies space between the base-centered lattice points and to a first approximation the diffuse scatter can be thought of as circles with their planes perpendicular to $\langle 111\rangle_f$ directions and their centers located at $\frac{1}{2}(2n + 1)\langle 111\rangle^*_f$ positions (shown schematically in Fig. 3. Comparison may be made with Fig. 2 and their two-dimensional symmetry elements given in Table I. The symmetry elements found agree with those that should be present in planes passing through the origin of a periodic object with space group $Im3m$, viz., a BCC lattice.

3.4. Origin of the Diffuse Scattering

Diffuse scattering in regions of reciprocal space between reciprocal lattice points may have one of two origins: The first possibility is that is a dynamic phenomenon due to the presence of a soft phonon mode, e.g., as a consequence of a martensitic transformation occurring at the observation temperature. High energy electrons interact with a crystal for a short time ($\sim 10^{-16}$ sec) and so experience effectively a static atom configuration. Alternatively, diffuse scattering may arise from static perturbations of the fluorite lattice caused by dislocations or local ordering.

The two possibilities may be distinguished by high resolution electron microscopy followed by optical diffraction of the resulting micrographs. The method is discussed by Tendeloo and Amelinckx (*19*) and

has been used to distinguish short-range ordering occurring in Au–Mn alloys and soft phonon modes in Cu–Zn–Al alloys.

Figure 4 shows a high resolution lattice image at the $\langle 110 \rangle_f$ pole. The micrograph shows subtle modulations of the lattice fringes on the scale of 20–30 Å. This is more clear if the figure is viewed at a grazing incidence: the rows of dots are not quite straight and the dot brightness fluctuates. A detailed interpretation of this micrograph has not been undertaken, rather it is included to show that there are irregular features in the periodicity which may be correlated with the diffuse intensity features observed in diffraction. Optical diffraction of this image reproduced both the Bragg reflections and the diffuse intensity, which originates from

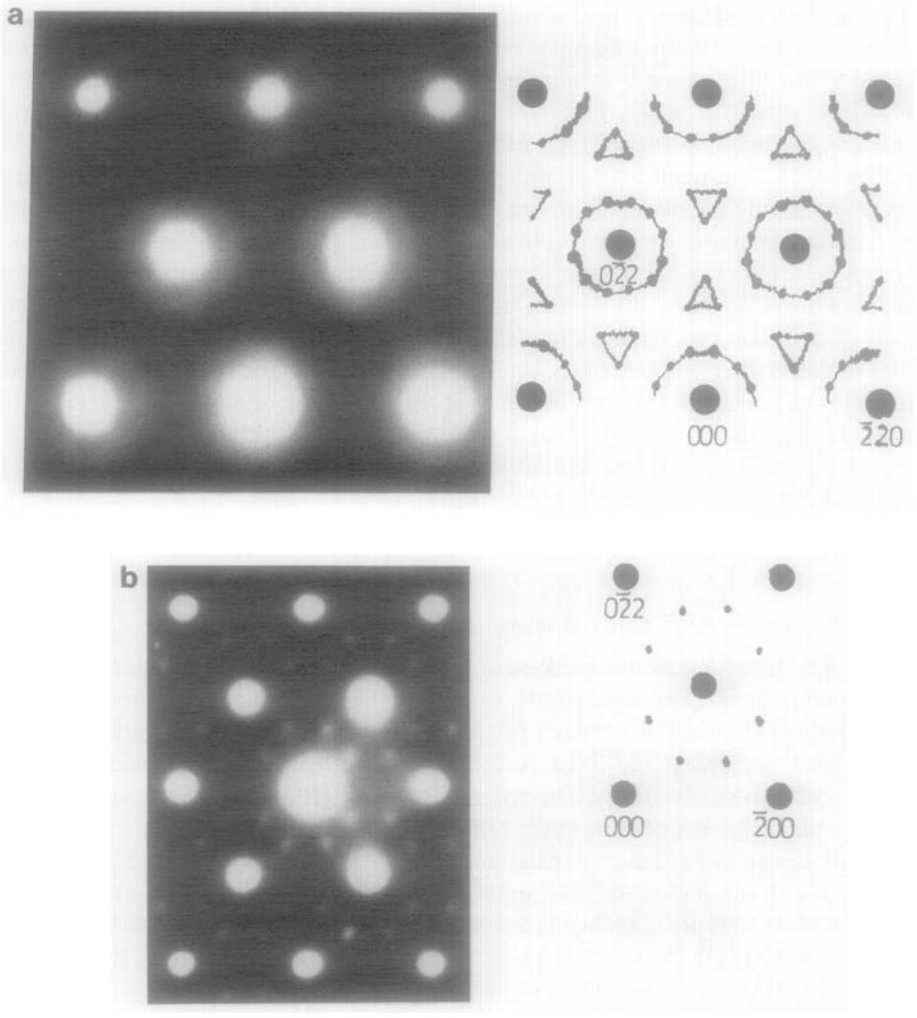

FIG. 2. Selected-area diffraction from a single crystals of urania-43% yttria. The overall appearance of each experimental diffraction pattern (a–e) is shown schematically in accompanying diagrams. The fluorite reflections are represented by large black circles. The position of the direct beam is annotated as are two other fundamental reflections. The diffuse scattering intensity that occurs between the nodes of the Bragg reflections is indicated. (a) $\langle 111 \rangle_f$, (b) $\langle 110 \rangle_f$, (c) $\langle 112 \rangle_f$, (d) $\langle 233 \rangle_f$, (e) $\langle 125 \rangle_f$.

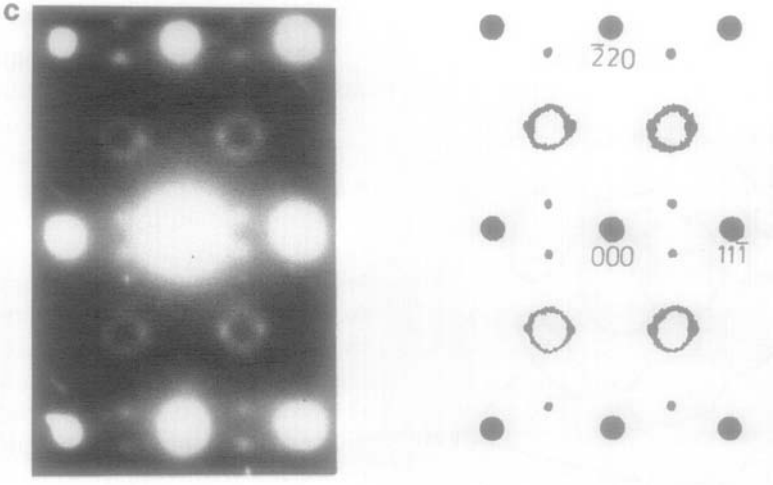
c
$\bar{2}20$
000
$1\bar{1}\bar{1}$

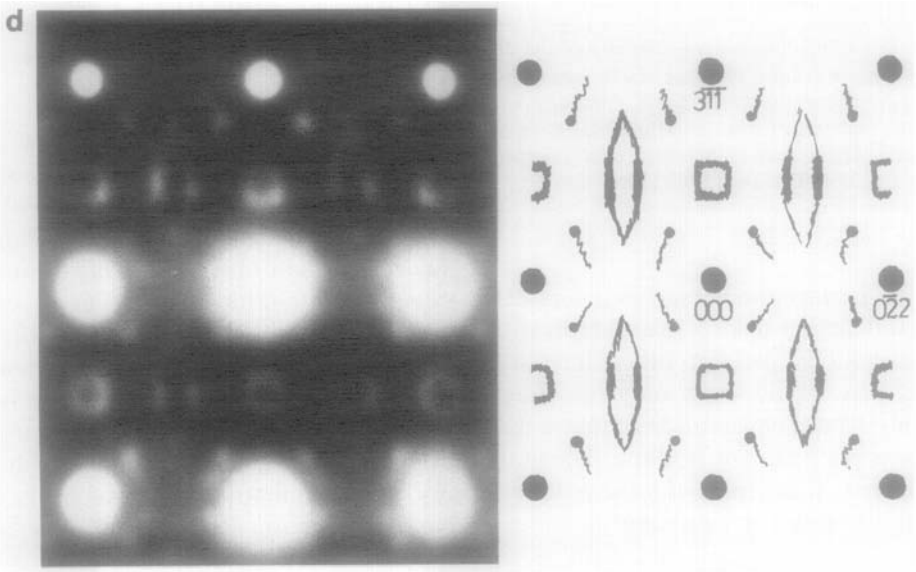
d
$3\bar{1}\bar{1}$
000
$0\bar{2}2$

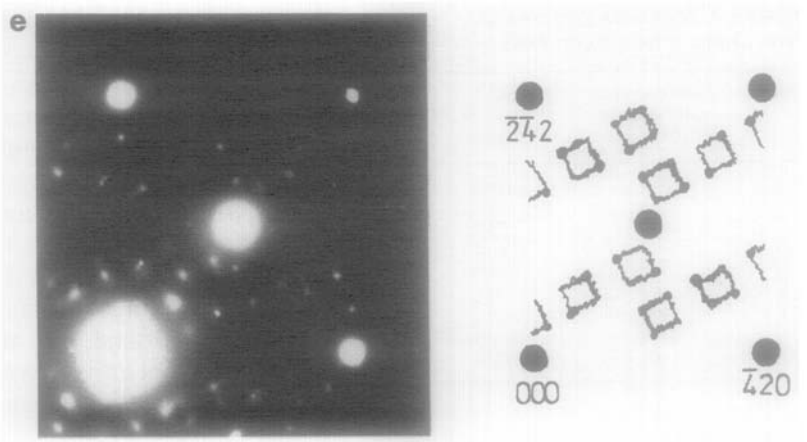
e
$\bar{2}\bar{4}2$
000
$\bar{4}20$

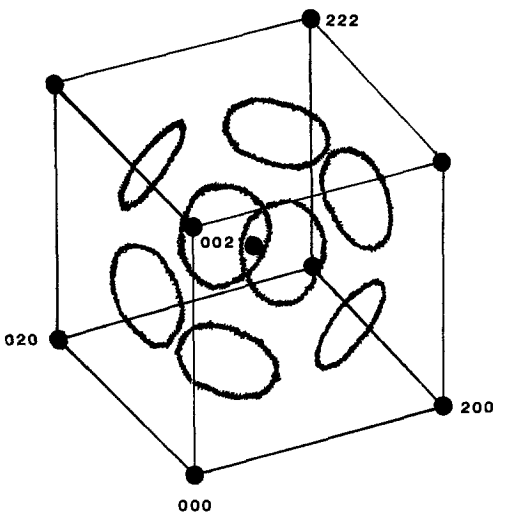

FIG. 3. The three-dimensional geometry of the diffuse scattering in reciprocal space. Each unit cell of reciprocal space contains two reciprocal lattice points per cell and eight equal rings of diffuse scattering arranged octahedrally in pairs with their planes perpendicular to the four equivalent $\langle 111 \rangle^*_f$ directions.

the lattice perturbations (see Fig. 4 inset). Optical diffraction from a micrograph with no perturbations present other than dynamic effects would show only the Bragg reflections. These observations confirm that the present phenomenon is static. The most likely cause is some form of local ordering; this could be short or long range.

TABLE I

TWO-DIMENSIONAL SPACE GROUPS OF FCC ELECTRON DIFFRACTION PATTERNS[a]

Type of plane normal (u,v,w without common factor)	Two-dimensional space group of diffraction pattern	Examples
$[00w]$	$p4m$	[001]
$[0vw]$	cmm	[011]
$[uuu]$	$p6m$	[111]
$[0vw] v + w = 2n + 1$	pmm	[012]
$v + w = 2n$	cmm	[013]
$[uuw] 2u + w = 2n + 1$	cmm	[122]
$2u + w = 4n + 2$	cmm	[114]
$2u + w = 4n$	pmm	[112],[116],[233]
$[uvw]$	$p2$	[125]

[a] Table after Ref. (*21*).

Diffuse intensity arising from ordering has also been observed in vanadium carbides and nitrides (*20*) and titanium oxides (*21*) for which an interpretation of short-range order was given (*22*). Measurements on the half-widths of the diffuse scattering intensity in the present case however show that the scattering centers are on the order of 20 to 30 Å in size. This is consistent with a dark field image taken in a $\langle 110 \rangle_f$ direction which shows mottled contrast on a scale of 30 Å (Fig. 5). These observations suggest the existence of a heterogeneous microstructure, indicating that a microdomain description may be more appropriate.

4. Simulation of the Diffuse Intensity in Urania-Yttria

We have attempted to identify the structure of the microdomains formed in urania-43% yttria using the approach of Allpress and Rossell (*9*). These authors developed a suite of programs used originally to simulate complex diffraction phenomena in calcia-stabilized hafnia. The programs (kindly supplied by Dr. Henry Rossell) were modified for the purposes of this work to run on the Oxford Vax Cluster. The method used in calculating these patterns including the theory and assumptions on which they are based is given in Ref. (*9*) and only a brief outline is given here. The diffraction of electrons from individual microdomains was assumed to be kinematic and the distribution of intensity about each reciprocal lattice point was assumed to be spherical, with a Gaussian profile. For large domain sizes dynamic effects will become significant. It is likely, however, that various orientations of a given microdomain in the fluorite matrix will present a range of thickness to the electron beam that will average out the dynamical effects in some complicated fashion. Allpress and Rossell found that this simple approximation did not introduce any serious discrepancies into their calculations and so

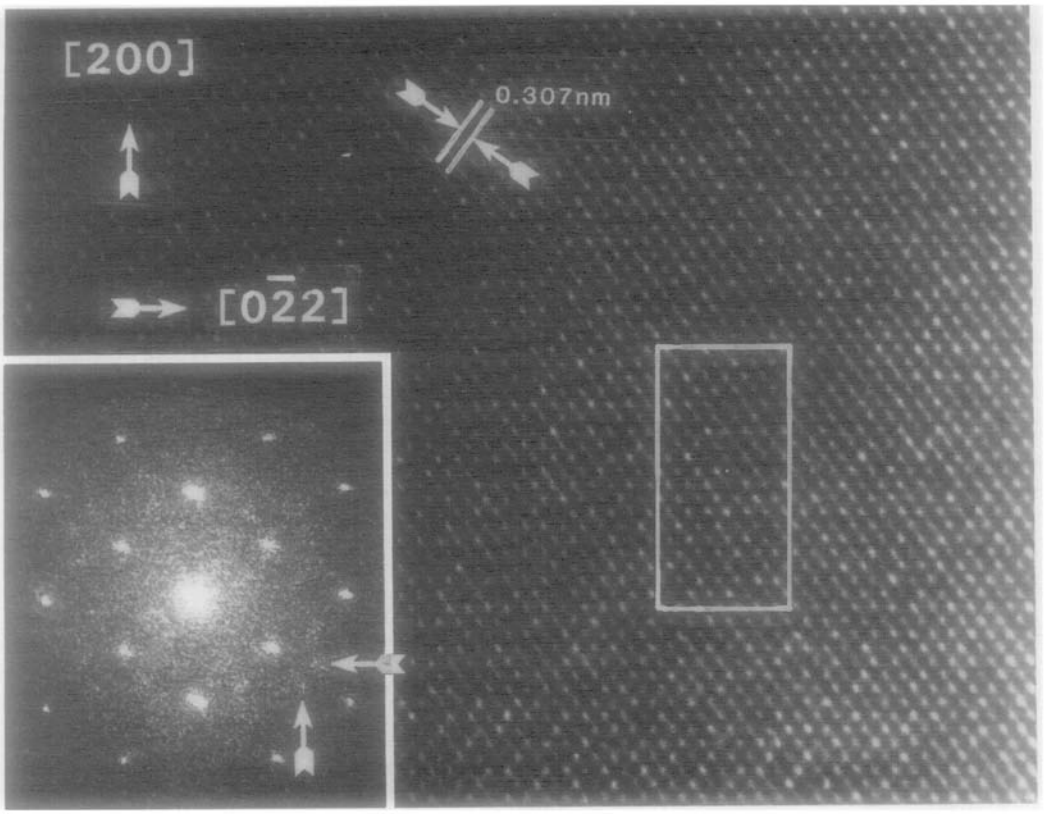

FIG. 4. Lattice image of urania-yttria on a $\langle 110 \rangle_f$ axis showing fringes corresponding to $\{111\}_f$ planes and irregular features in contrast (outlined). The diffuse maxima reproduced by optical diffraction are indicated by arrows (cf. inset with Fig. 2b).

this approximation is used here. The effects of double diffraction were taken into account by translating each quadrant of the reciprocal lattice plane under consideration, so that their origins coincided with each subcell reflection in turn, and summing the intensity contribution at each point. The subcell reflections in these double diffraction calculations were assumed to have the same intensity as the direct beam and were therefore given equal weight. The supercell reflections were not considered as sources of double diffraction because their intensities were very small by comparison with the subcell reflections.

We have used the program to simulate the expected diffuse scattering intensity of small microdomains with a number of candidate fluorite-related structures embedded in a fluorite matrix. The microdomain structures that were examined included the rhombohedral structure UY_6O_{12}; α-U_3O_8 and its high temperature modification β-U_3O_8; and UY_4O_9 adopting the ϕ_1 structure (i.e., uranium and yttrium respectively substituted for calcium and hafnium). The related tungsten–yttrium–oxygen system was also explored and possible structures considered were the polymorphs α-YW_2O_6 and ε-YW_2O_6.

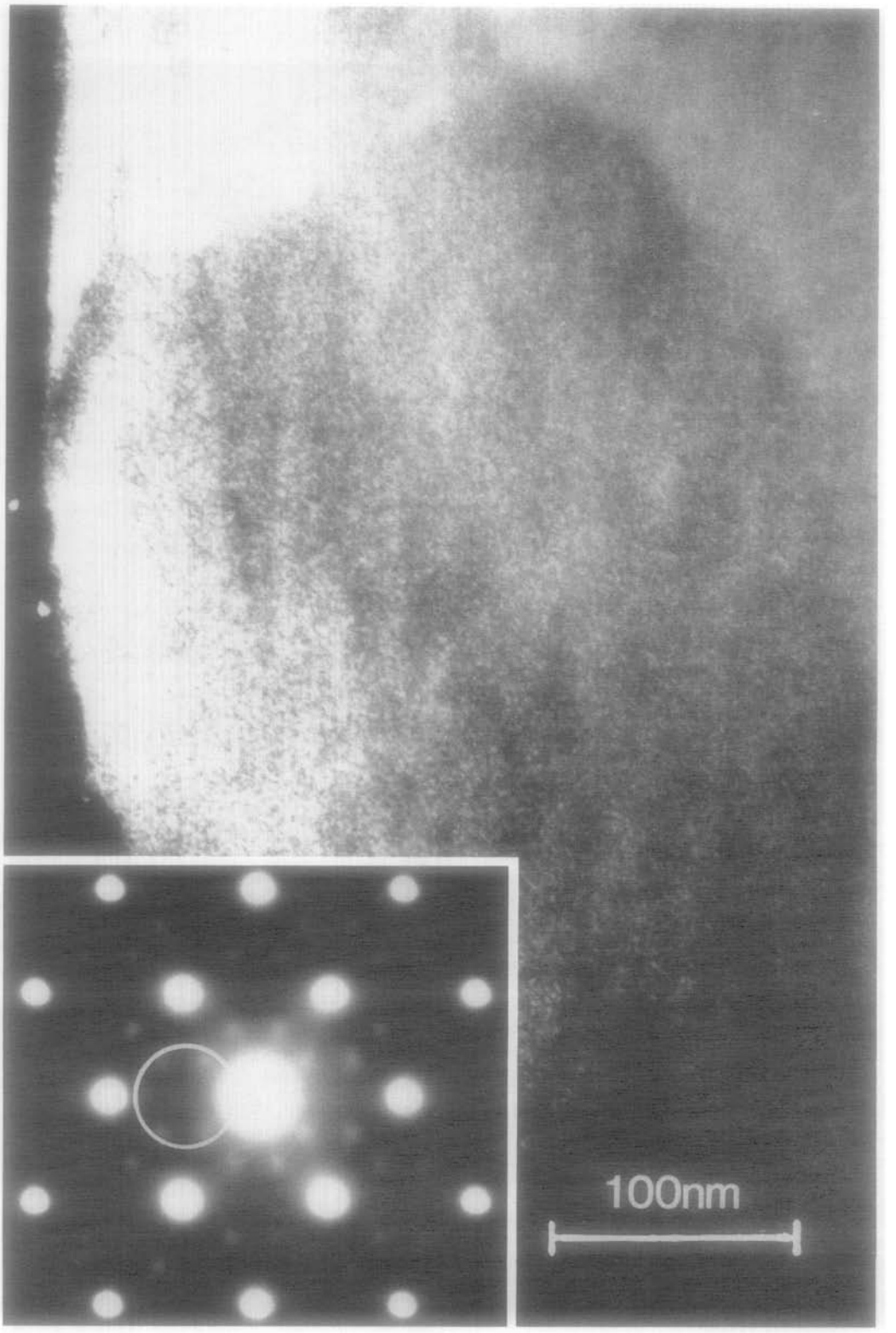
100nm

ϕ_1 Microdomains

Allpress and Rossell (*9*) found that a model with 30-Å diameter domains of $CaHf_4O_9$, with the ϕ_1 structure, embedded in a fluorite matrix was found to agree with their experimental diffraction data in calcia-stabilized hafnia. The axes of the unit cell of ϕ_1 are related to those of the fluorite unit subcell by the expression

$$\begin{pmatrix} a \\ b \\ c \end{pmatrix}_{\phi_1} = \begin{pmatrix} 2 & 2 & 2 \\ -2 & 2 & 0 \\ -\frac{3}{2} & -\frac{3}{2} & 1 \end{pmatrix} \begin{pmatrix} a_1 \\ a_2 \\ a_3 \end{pmatrix}_f . \quad (1)$$

The program suite was tested by using data for lime-hafnia and it was found to reproduce Allpress and Rossell's calculations, thereby confirming that the programs functioned correctly.

Electron diffraction patterns arising from domains within urania-43% yttria and published patterns of calcia-stabilized hafnia show some remarkable similarities, suggesting perhaps models based on the ϕ_1 structure may be applicable in both cases. However, the ϕ_1 structure is not known in the urania-yttria system. A plausible ϕ_1 structure is obtained by substituting the calcium ions for uranium ions and the hafnium for yttrium so that the stoichiometry UY_4O_9 would be adopted. In order for this to occur the uranium ion would have to be in the hexavalent state. The simulations for this structure obtained for the $\langle 110 \rangle_f$, $\langle 233 \rangle_f$, and $\langle 112 \rangle_f$ poles are shown in Figs. 6a to 6c. The results were essentially the same as those obtained for $CaHf_4O_9$: Some diffuse features were slightly brighter in the simulation for "UY_4O_9" but the morphology of the diffuse scattering remained unchanged. These observations are a consequence of the different scattering factors involved. The relative scattering power of the cations in $CaHf_4O_9$ to those in UY_4O_9 is 308/248 = 1.2.

However, on comparing these calculations based on UY_4O_9 with the experimental results, there are some significant differences in the morphology of the diffuse intensity. For instance, in the case of the $\langle 110 \rangle_f$ zone axis, the distance between similar diffuse maxima relative to a $\langle 220 \rangle^*_f$ vector is different in the two cases: In the experimental pattern at the $\langle 110 \rangle_f$ pole (Fig. 2b) the distance "a" is larger than "b", but for ϕ_1 ordering in the same zone axis (Fig. 6a), however, $b > a$. In the $\langle 233 \rangle_f$ zone axis the circular diffuse features are centered at $\frac{1}{2}(m + 1)\langle 311 \rangle^*_f + n\langle 220 \rangle^*_f$ positions. In the experimental diffraction pattern (Fig. 2d) they appear quasi-square whereas in the ϕ_1 calculation (Fig. 6b) they appear quasi-hexagonal. Furthermore, for ϕ_1 ordering, the apparent diameter of these shapes is a larger fraction of the $\langle 220 \rangle^*_f$ vector than in the experimental case. The distinct smoke ring that appears in the $\langle 112 \rangle_f$ pole (Fig. 2c) located at $\frac{1}{2}(n + 1)\langle 311 \rangle^*_f$ positions also appears in the $\langle 112 \rangle_f$ pole for ϕ_1 (Fig. 6c) centered in the same locations. However, although the apparent diameter of this diffuse feature is similar in the two cases, the positions of the diffuse maxima are not. In the former case the maximum occurs along the $\langle 111 \rangle^*_f$ direction while it occurs along a $\langle 220 \rangle^*_f$ direction in the latter. These differences are sufficiently significant to rule out ϕ_1 ordering in urania-yttria.

RhI Microdomains

The choice of RhI for further calculations was made on the following grounds: The lattice parameter of urania-43% yttria air-annealed at 1600°C was found to be 5.313 Å and the ideal RhI lattice parameters were *a*

FIG. 5. Dark-field image of urania-yttria showing mottled contrast on a scale of ~30 Å. The image was constituted from the diffuse intensity occuring in a diffraction pattern of the $\langle 011 \rangle_f$ zone axis (see inset).

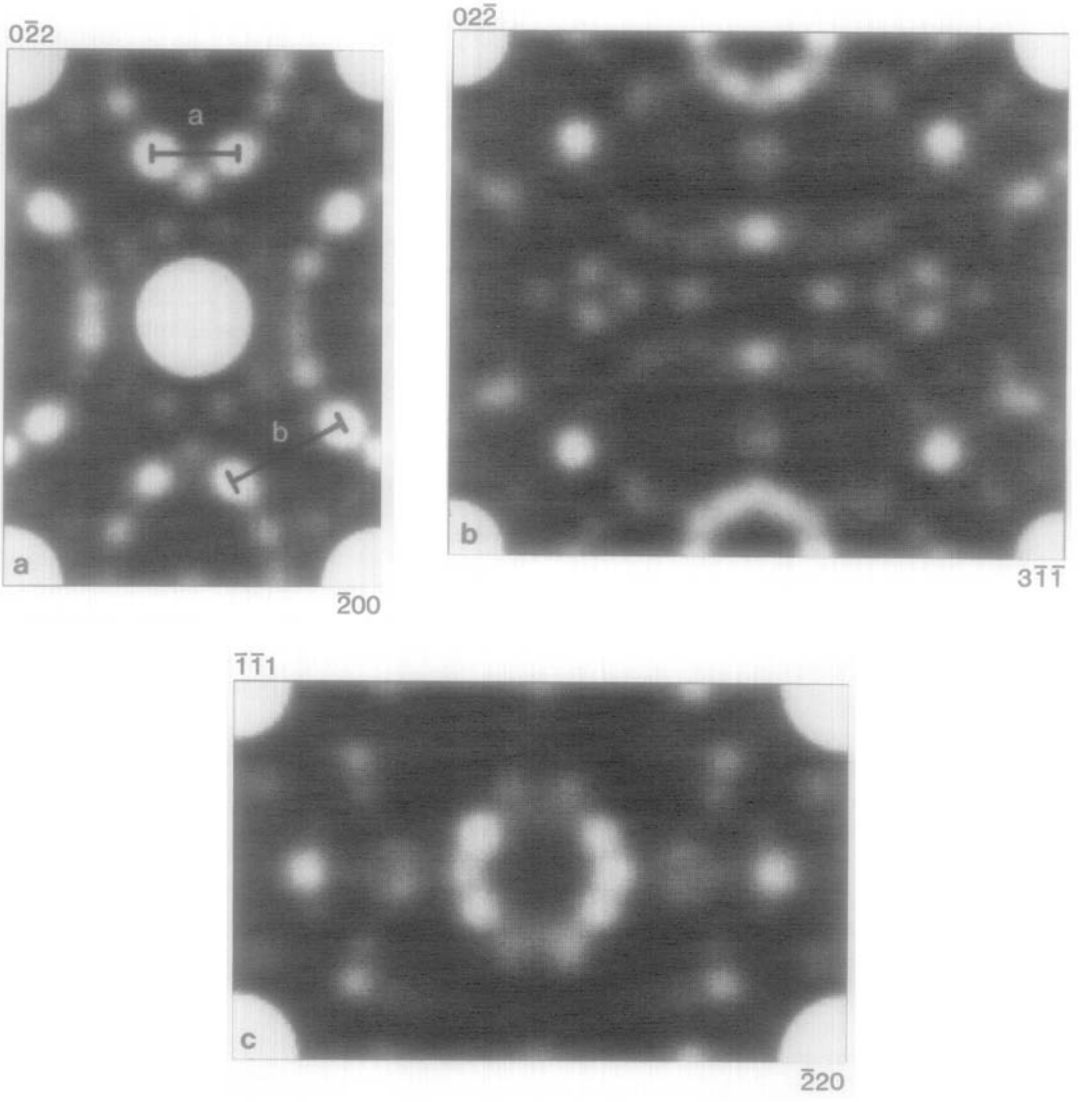

FIG. 6. Computed halftone electron diffraction pattern for ϕ_1 domains embedded in a urania-yttria matrix. In (a) to (c) are shown patterns expected from a structure consisting of domains of ordered ϕ_1, 30 Å in diameter; the domains occur in 12 different orientations with respect to the fluorite-type matrix; subcell reflections lie at the corners of each pattern and at the center of the $\langle 110 \rangle_f$ pattern. (a) $\langle 110 \rangle_f$, (b) $\langle 233 \rangle_f$, (c) $\langle 112 \rangle_f$.

= 6.507 Å and α = 99.59° as calculated from Eq. (2) below (*2*),

$$\begin{pmatrix} a \\ b \\ c \end{pmatrix}_{\text{RhI}} = \begin{pmatrix} -\frac{1}{2} & \frac{1}{2} & 1 \\ \frac{1}{2} & 1 & -\frac{1}{2} \\ 1 & -\frac{1}{2} & \frac{1}{2} \end{pmatrix} \begin{pmatrix} a_1 \\ a_2 \\ a_3 \end{pmatrix}_f . \quad (2)$$

The corresponding values for UY_6O_{12}, fully oxidized RhI, are a = 6.530 Å and α = 99.05°. This indicates that distortion introduced by the ordering of cations and vacancies on the superlattice of RhI is small (disregistry ~$\frac{1}{2}$%). Furthermore, the overall

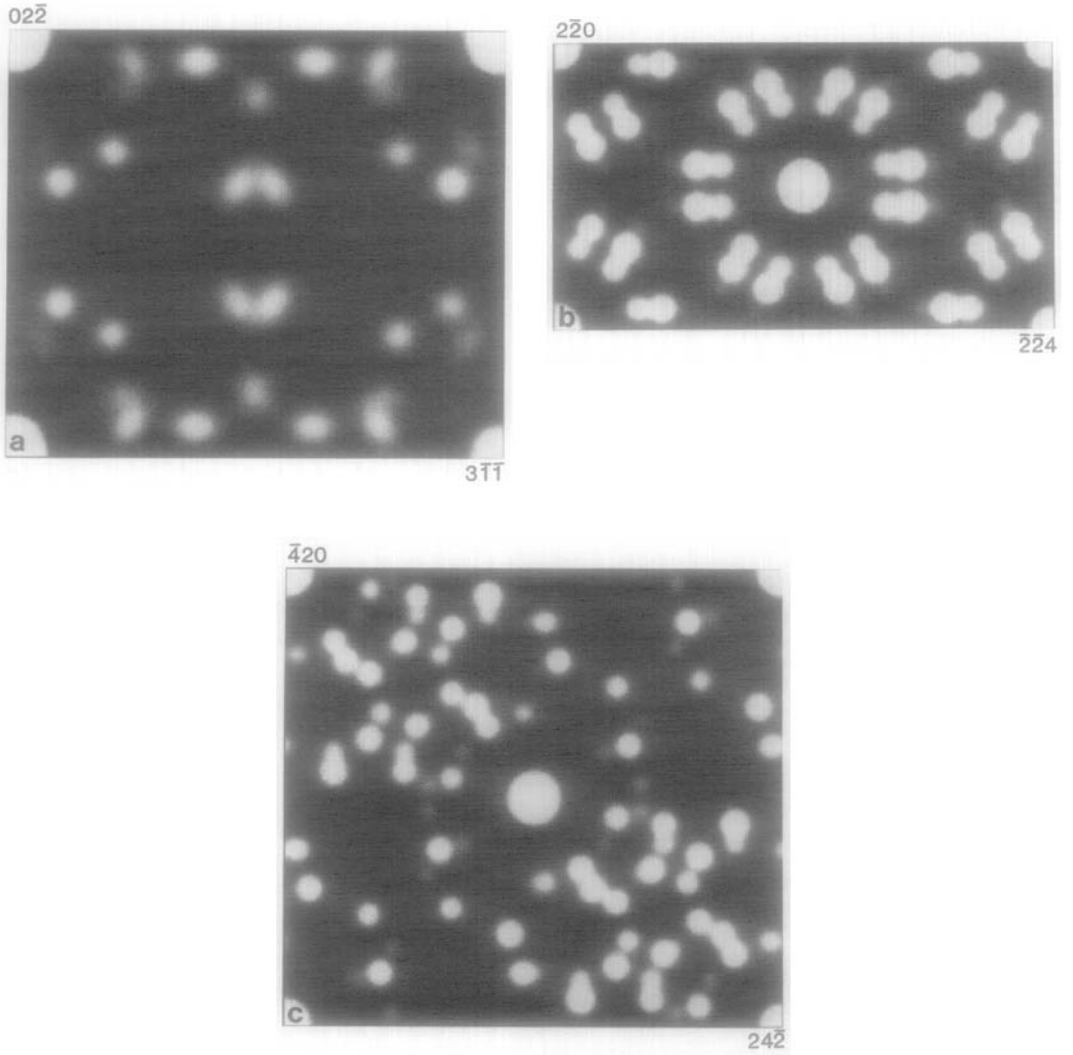

FIG. 7. Computed halftone electron diffraction pattern for RhI domains embedded in a urania-yttria matrix. In (a) to (c) are shown patterns expected from a structure consisting of domains of ordered RhI, 30 Å in diameter; the domains occur in eight different orientations with respect to the fluorite-type matrix; subcell reflections lie at the corners of each pattern and at the centers of the $\langle 111\rangle_f$ and $\langle 125\rangle_f$. (a) $\langle 233\rangle_f$, (b) $\langle 111\rangle_f$, (c) $\langle 125\rangle_f$.

stoichiometry of the oxidized powder $MO_{2.058}$ compares favorably with the stoichiometry of the RhII structure of $MO_{1.9}$. It would thus be expected that domains of the RhI phase could exist in a fluorite-type matrix without introducing large strains, at least for small domain sizes. The presence of RhI domains therefore seemed a plausible explanation for the occurrence of complex diffraction phenomena observed in urania yttria. Figures 7a–7c show halftone plots for the $\langle 233\rangle_f$, $\langle 111\rangle_f$, and $\langle 125\rangle_f$ poles for 30 Å diameter RhI microdomains. It can be seen that there is considerable disparity between

these simulations and the corresponding experimental diffraction patterns (Figs. 2d, 2a, and 2e, respectively). This is particularly clear in the case of the $\langle 233 \rangle_f$ pole (Fig. 2d) and the $\langle 125 \rangle_f$ pole (Fig. 2c). In the $\langle 233 \rangle_f$ simulation the distinct quasi-square features that are observed experimentally are not reproduced and the $\langle 125 \rangle_f$ zone axis simulation did not duplicate the small quasi-squares seen experimentally. The best fit with this model seems to be down the $\langle 111 \rangle_f$ pole. However, careful measurement of the relative ratios of supercell reciprocal lattice vector magnitudes and intervector angles are inconsistent with each other and so RhI is not the ordering scheme here.

Other Possible Structures

A number of other possible structures for the microdomains were tried: orthorhombic U_3O_8 type structures which constitute the only other known phases in the UO_2–Y_2O_3–UO_3 system; and phases which occur in the related Y_2O_3–$Y_2O_3 \cdot WO_3$ system. None of these gave any agreement with the experimental diffraction patterns.

5. Observations of Microdomains in Urania-Ceria

5.1. X-Ray Diffraction Observations

X-ray diffractometry showed that the solid solutions did not stray from Vegards' law in the experimental range of cerium concentration $(U_{1-y}, Ce_y)O_{2-x}$ with $y = 0.2$, 0.4, and 0.6. The lattice parameter of the solid solutions decreases linearly with increasing cerium concentration (Table II).

This observation also agreed with that of Markin and coworkers (*23*). It also showed that cubic, single-phase solid solutions with the fluorite structure were formed for all powders in this study. However, solid solutions with values of ceria content corresponding to $y = 0.4$ and $y = 0.6$ both exhibited in their powder diffraction patterns a broad feature, at an angle of $2\theta_B = 14.1°$, in addition to the Bragg peaks expected for a fluorite structure (Fig. 8). This broad feature is at a much lower angle than the first Bragg peak, $\{111\}_f$, which occurs at a $2\theta_B$ angle of 29.4°. The average size of the scattering centers attributable to this hump can be estimated using the Scherrer particle size equation giving the approximate particle size as ~21 Å. This value is consistent with the one obtained from electron microscope observations discussed below.

TABLE II

URANIA-CERIA LATTICE PARAMETERS

Cerium content (at %)	Lattice parameter[a] (Å)	Color of powder
0.0	5.4719(5)	Brown/black
20.0	5.4595(5)	Black
40.0	5.453(6)	Black
60.0	5.439(1)	Black

[a] Bracketed term gives standard deviation on last figure.

X-ray diffractometry of urania-60% ceria air-annealed at 1600°C showed a decrease in lattice parameter with a value of 5.4262(7) Å compared with the powder as supplied which had a lattice parameter of 5.439(1) Å. Also no broad features were observed at low Bragg angles.

5.2. Electron Microscopy Observations

The samples of urania-ceria containing 20 mole% and 60 mole% ceria were studied in the electron microscope as they showed different features in X-ray diffraction. In urania-20% ceria the predominant features that were found were dislocations, whereas in urania-60% ceria ordering was seen in the form of small heterogeneities that appear coherent with the matrix.

High-resolution structure images of single crystals of urania-20% ceria showed a het-

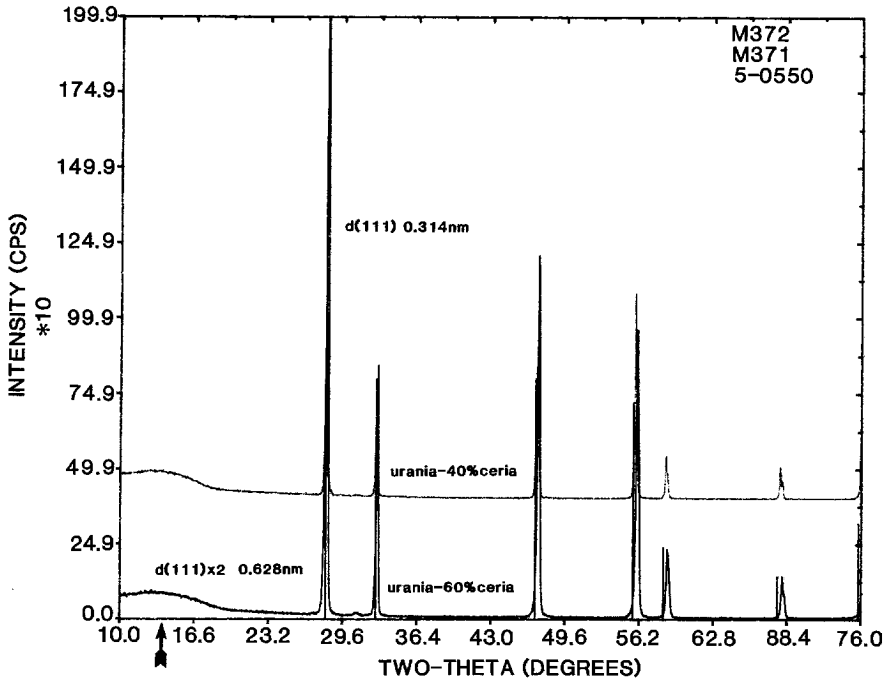

FIG. 8. X-ray powder diffraction from urania-ceria. The 111_f fluorite peak of urania-60% ceria is indicated. A broad feature is loated at an angle of $2\theta_B = 14.1°$.

erogeneous distribution of dislocations. The dislocations were not homogeneously distributed as the dislocation density varied from crystal to crystal. In some crystals densities as high as 10^{16} m^{-2} were estimated to have been present whereas in others no dislocations at all were found. All of the dislocations which have been analyzed have Burgers vectors consistent with the type $\mathbf{b} = \frac{1}{2}\langle 110\rangle_f$ in projection (Fig. 9).

Structure images of single crystals of $(U_{0.4}, Ce_{0.6})O_{2-x}$ solid solution showed an apparent local doubling of the $\{111\}_f$ lattice fringe spacing when viewed in a $\langle 110\rangle_f$ orientation (Fig. 10a). This effect is subtle, but it is more apparent in thicker regions of crystal or in thin areas at a high value of defocus. It was seen in all crystallites and in all foil thicknesses. The effect seen in the lattice structural image (Fig. 10a) cannot be attributed to symmetry-breaking due to the crystal being "off-axis" or to poor beam alignment. This is because centrosymmetry of the lattice fringes is preserved in thin regions of crystal (*24*) both at Scherzer defocus and at higher defocus values. If departure from centrosymmetry were attributable to this then the whole crystal would be affected in the same way, unless the foil were severely bent. Therefore these effects seen in lattice images are due to domains of a second phase.

In the corresponding SAD pattern (Fig. 10b) at this crystal orientation this "doubling effect" could be correlated with "rice grain" shapes of diffuse intensity located at $\frac{1}{2}\langle 111\rangle_f^*$ positions. Although these diffuse features were weak they were reproduced by optical diffraction of the HREM micrograph and so are not due to thermal diffuse scattering. The fact that this ordering appears as small blobs rather than sharp dif-

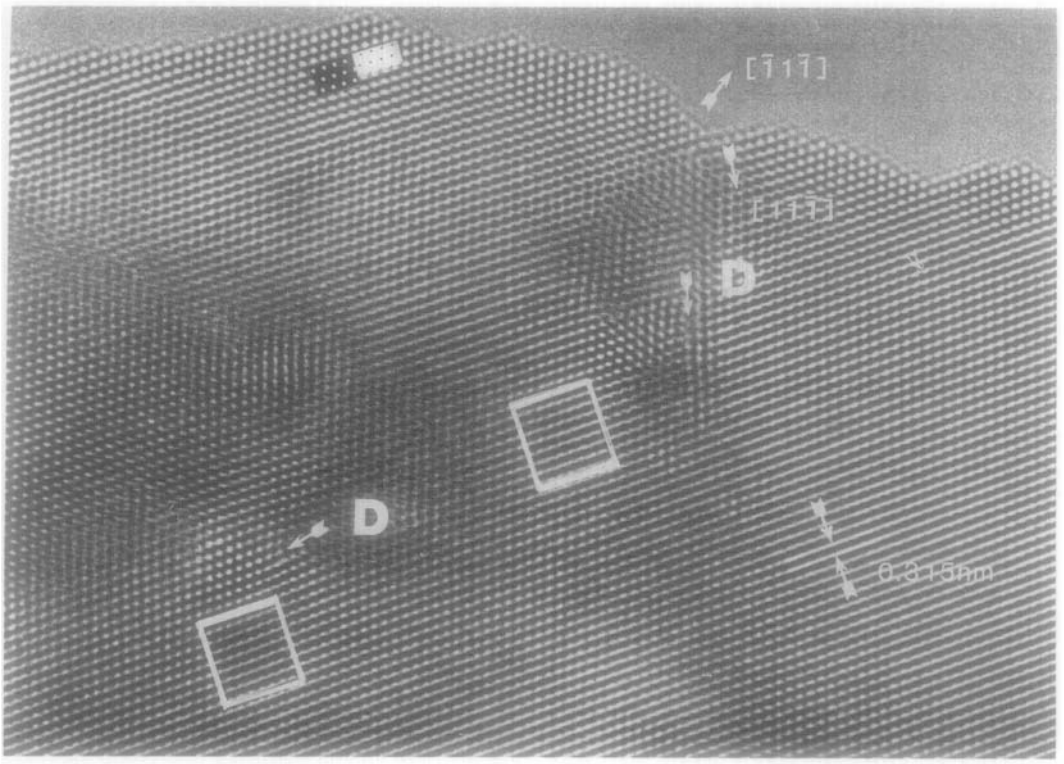

FIG. 9. High resolution lattice image of urania-20% ceria in a $\langle 110 \rangle_f$ orientation. The micrograph was taken at Scherzer defocus; The inset at the top left of the figure shows an image simulation, and the corresponding projected potential, illustrating that the "center of gravity" of the black blobs in the lattice image represent columns of cations. Approximate locations of dislocation cores causing bending of neighboring crystal planes (outlined) are noted (D). This is manifested by symmetry breaking of the lattice fringes.

FIG. 10. (a) High-resolution lattice image of urania-60% ceria in a $\langle 110 \rangle_f$ orientation taken at Scherzer defocus ($\Delta f = -405$ Å). The micrograph shows a subtle modulation of the 111_f planes. This is clear if the figure is viewed at a glancing incidence. One can see a "doubling" of the $(\bar{1}11)$ periodicity if the micrograph is viewed in a direction indicated by the arrows in the planes marked A and a doubling of the $(\bar{1}1\bar{1})$ periodicity if the micrograph is viewed in a direction indicated by the arrows at B. (b) Selected-area diffraction from a single crystal of urania-60% ceria on $\langle 110 \rangle_f$. In addition to reflections from the fluorite planes, "rice grain" shapes of diffuse intensity occur at $\frac{1}{2}\langle 111 \rangle^*_f$ positions. One such feature is arrowed. (c) Optical diffraction from HREM micrograph of urania-60% ceria on $\langle 110 \rangle_f$. This optical diffractogram, which was taken from Fig. 10(a), reproduces the matrix reflections and the rice grain shapes observed in the experimental diffraction pattern Fig. 10(b).

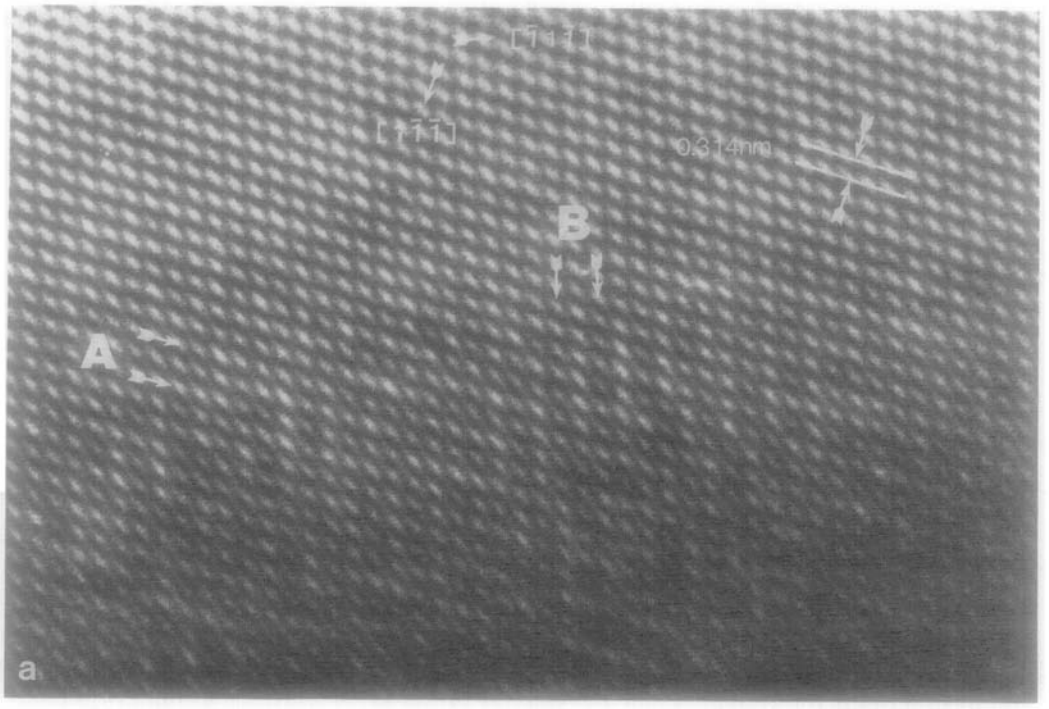
[1̄11]
[11̄1]
0.314nm
B
A
a

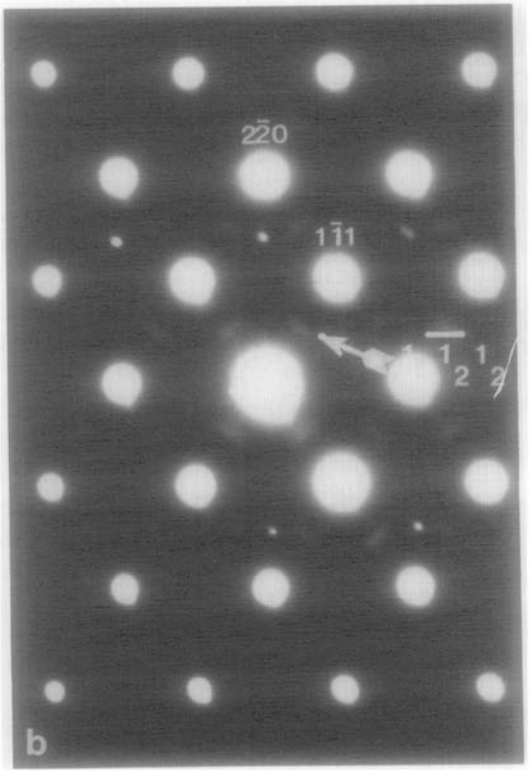
2̄20
1̄11
1/2 1/2
b

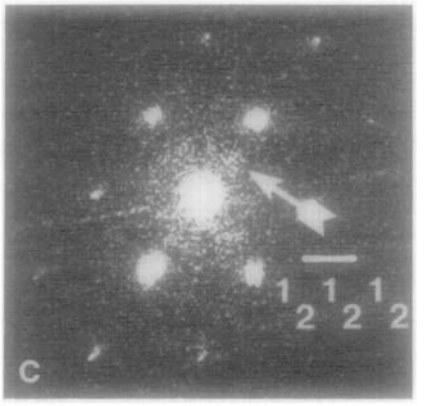
1/2 1/2 1/2
c

fracted spots agrees with the observation in the lattice image that the ordering occurs in small domains (of sizes 15–30 Å) rather than throughout the whole crystal. Similar electron diffraction observations have been seen by Herrero and Rojas (*25*) in the U–Ca–La–O system although no explanation was offered. All these observations are consistent with our X-ray diffraction experiments.

Diffraction patterns at the $\langle 112 \rangle_f$ pole showed weak spots located at $\frac{1}{2}\langle 113 \rangle_f^*$ positions. These cannot be attributed to reflections from a higher order Laue zone as such reflections would occur in $\frac{m}{2}\langle 220 \rangle_f^* + \frac{n}{3}\langle 111 \rangle_f^*$ ($m \neq 3p$, $n \neq 3p$, where m, n, and p are integers) positions. Lattice images at this zone axis did not show any evidence of planar modulation. The diffuse features seen in the diffraction patterns are considerably weaker than the complex diffraction phenomena seen in urania-yttria and were not seen in other zones. Attempts at dark field imaging using these extra reflections proved unsuccessful. Exposure times in excess of a minute were necessary for magnifications of 100K × and the effects of specimen drift proved to be excessive.

5.3. Interpretation of Observations in Urania-Ceria

The main features of the electron diffraction patterns are rice grain shapes located at $\frac{n}{2}\langle 111 \rangle_f^*$ positions in the $\langle 110 \rangle_f$ diffraction patterns and weaker diffuse features located at $\frac{n}{2}\langle 131 \rangle_f^*$ positions in the $\langle 112 \rangle_f$ diffraction pattern. For the $\langle 110 \rangle_f$ zone axis these rice grains correspond to a doubling of the $\{111\}_f$ periodicity consistent with the lattice image observations (Fig. 10a). Only an approximate picture of the three-dimensional geometry can be obtained. As in urania-yttria, the features seen in urania-ceria diffraction patterns can be described by the symmetry elements of the *Im*3*m* space group. They consist of "disks" of diffuse intensity with the "center of gravity" of each disk located at $\frac{n}{2}\langle 111 \rangle_f^*$ positions and with their planes perpendicular to $\langle 111 \rangle_f^*$. The dimensions of the disks, measured from the rice grain half-widths are a diameter of 0.07 $Å^{-1}$ and a thickness of 0.036 $Å^{-1}$. In real space this corresponds to rod-shaped domains having a diameter of ~14 Å and an axial length of ~28 Å with their axes aligned along $\langle 111 \rangle_f$ directions.

A possible explanation, consistent with these observations, is that the microdomains have the fluorite-related pyrochlore structure having space group *Fd*3*m* (No. 227). The pyrochlore structure can be derived from the parent fluorite structure by juxtaposing eight fluorite cells to form a larger cubic cell and removing $\frac{1}{8}$ of the oxygen ions in a systematic fashion (*26*). As the real space lattice is also face-centered cubic the reciprocal lattice will be body-centered cubic but with all linear dimensions halved because the pyrochlore lattice parameter is double that of fluorite. The positions of the diffracted spots for pyrochlore are consistent with those experimentally observed. Pyrochlore-type superstructure peaks have been observed previously in mixtures of Y_2O_3–ReO_2 (*27*) and La_2O_3–WO_3 (*28*). The radius ratios of the cations, $r(M^{3+}) : r(M^{4+})$ are 1.27 for the yttria–rhenia mixture and 1.24 for the lantha–tungsten mixture. These figures were calculated using Ahrens radii (*29*). Pyrochlore structures have also been observed in a series of stannates $A_2Sn_2O_7$ (*30*) (where A = Y, Sm, La). Limits have been put on the cation radius ratio for pyrochlore formation in stannates and these range from 1.19 to 1.6. The stability field of pyrochlore in these materials could be extended by the use of high pressure (65 kbars) so that the upper limit was increased to 1.8 (*31*). Pyrochlore formation is not

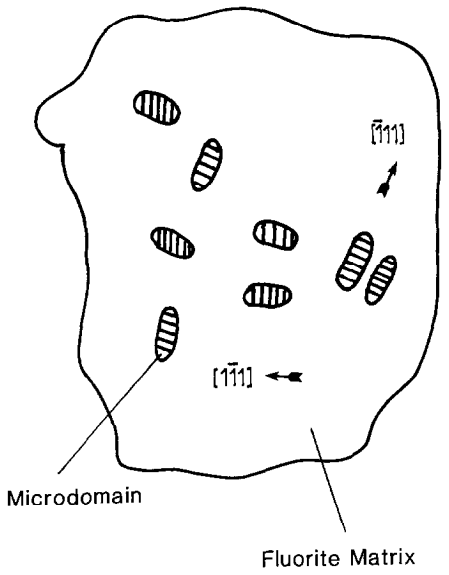

FIG. 11. Microdomain model for urania-ceria. Coherent domains of partially ordered pyrochlore. Each domain is partially ordered on one set of 111_f planes and is elongated in a direction perpendicular to the ordered plane.

known in the urania–ceria system but its formation is not out of the question; the cation radius ratio, $r(Ce^{3+}):r(U^{4+})$ is 1.16 which is just below the range expected for pyrochlore formation.

The rice grain shapes observed in electron diffraction (Fig. 10b) suggests that the pyrochlore microdomains are elongated in $\langle 111\rangle_f$ directions. It can be concluded from this that the ordering in urania-ceria may be partial; in a given microdomain one set of $\{111\}_f$ planes are more strongly ordered than the other $\{111\}_f$ planes. These ordered planes occur longitudinally in each domain. This idea is illustrated schematically in Fig. 10. This may be due to the fact that the cation radius ratio is below the limit for fully ordered pyrochlore formation.

6. Discussion and Conclusion

XRD, HREM, and SAD studies have shown that the crystal structures of the mixed uranium oxides $(U_{0.4}, Y_{0.6})O_{2\pm x}$ and $(U_{1-y}, Ce_y)O_{2\pm x}$, where $y = 0.2, 0.4, 0.6$ are substantially of the fluorite type but that the structure is modified to accommodate deviations from the ideal stoichiometry ($MO_{2.0}$) by the incorporation of a variety of types of microdomains.

Evidence for microdomains in the urania–yttria system has been provided by the presence of extensive diffuse scattering in the selected area electron diffraction patterns. It has not been possible to determine the structure of the microdomains in urania-yttria explicitly but under general considerations one can deduce the likely primitive Bravais lattice to which the microdomains belong.

From calculations of the "spot" patterns expected for microdomains of various Bravais lattice types (Section 4) the following is evident: The lower the symmetry of the Bravais lattice the higher is the density of supercell reflections. This trend arises because lower symmetry structures can be fitted into the fluorite matrix in more equivalent orientations. We may attempt to quantify these remarks and thereby deduce the likely Bravais lattice class responsible for producing the diffuse maxima observed in urania-yttria.

It has been found that the observed diffraction patterns (Fig. 2) and the diffuse intensity maxima are consistent with the symmetry groups expected from sections through a BCC reciprocal lattice since they obey the two-dimensional space groups derived from the *Im3m* space group listed in Table I. It therefore follows that if the observed diffraction patterns are consistent with sections through a BCC lattice, the three-dimensional geometry of the diffraction patterns, i.e., the unit cell depicted in Fig. 3, can be described by the symmetry elements of the *Im3m* space group (*32*). Proceeding in this manner, the fluorite or subcell reflections can be assigned the 2(*c*) positions (000 and $\frac{111}{222}$) and the diffuse intensity

maxima or supercell reflections can be assigned the 96(l) general positions.

These symmetries arise because the domains occur in all crystallographically equivalent orientations. Since in urania-yttria the domain sizes are small (~30 Å) and the domain density is high, it can be assumed all domain orientations are present in a given selected-area electron diffraction pattern and indeed this must be the case, in general, if the $Im3m$ symmetry is preserved.

Consider the most general case of a triclinic superstructure embedded in a fluorite matrix. The orientation of triclinic planes with respect to the matrix can be generally described as $(100)_t \parallel (h_1k_1l_1)_f$, $(010)_t \parallel (h_2k_2l_2)_f$ and $(001)_t \parallel (h_3k_3l_3)_f$. Given one set of planes, say $(h_1k_1l_1)_f$, the others, $(h_2k_2l_2)_f$ and $(h_3k_3l_3)_f$, are uniquely defined by the interplanar angles α, β, and γ. Since the multiplicity of planes $\{hkl\}_f$ in the most general case (h, k, l all different) in a cubic system is 48 there will be 24 ways of orientating a triclinic Bravais lattice in a cubic matrix, since the multiplicity of a plane in a triclinic cell is 2. This is consistent with the idea developed in the previous paragraph that the diffuse intensity maxima, in general, can be assigned the 96(l) positions of the $Im3m$ space group. Since the BCC reciprocal lattice cell is nonprimitive, having two fluorite reciprocal lattice points per BCC cell, the maximum number of points generated by the $Im3m$ symmetry operators in a primitive cell is 96/2 = 48. The coordinates xyz of the supercell reflections as a fraction of the $\langle 200\rangle^*_f$ vector of the BCC reciprocal lattice cell can be deduced from microdomain–matrix relationships (expressions similar to Eqs. (1) and (2)). Coordinates generated by the $Im3m$ symmetry elements are given in the International Tables and if the microdomain has a triclinic Bravais lattice, all 96(l) positions are produced for any reflection type. If fewer than 96 positions are generated from a given xyz, due to positions mapping on one another, then it follows that the Bravais lattice is of a higher symmetry. If, however, a particular plane of the triclinic supercell is aligned parallel to a fluorite plane of low multiplicity, say $(100)_t \parallel (100)_f$ where this cubic plane has a multiplicity of 6, then clearly fewer spots will arise. In this case the $(100)_t$ spots will occur along the $(100)_f$ line. Consider the $(011)_f$ reciprocal lattice plane (Fig. 2b): measurements of the coordinates xyz of one of the diffuse maxima expressed as a fraction of a $\langle 200\rangle^*_f$ vector yield $x \approx 0.39$, $y \approx -0.26$ and $z = -y$. This maximum is related to the seven other maxima in this quadrant of the $(011)_f$ plane by the symmetry elements: $\bar{x}yz$, $\bar{x}\bar{y}\bar{z}$ and $xyz + \frac{111}{222}$, $\bar{x}yz + \frac{111}{222}$, $\bar{x}\bar{y}\bar{z} + \frac{111}{222}$ and since all maxima are strong it is assumed that the reciprocal lattice points to which they correspond lie in this plane, i.e., the deviation parameter is zero. There are a total of six different $\{110\}_f$ planes in a cubic lattice, and so it follows that there are a total of 8 × 6 diffuse intensity maxima with the above coordinates. This is also evident from the fact that the symmetry element $x\bar{z}\bar{y}$ leaves the coordinates xyz invariant. This means that there are a total of 24 reflections in the primitive reciprocal lattice suggesting that the microdomain may possess a higher symmetry than triclinic since the positions of the supercell spots are inconsistent with a triclinic cell having one of its planes parallel to a fluorite plane of high symmetry. Introducing a mirror plane to a triclinic Bravais lattice would force it to adopt monoclinic symmetry, i.e., a unique plane having "stacking vectors" normal to it. This would therefore reduce the number of general reflections in the BCC reciprocal lattice to a maximum of 48, which is consistent with the number of positions obtained above from the measurement of experimental diffraction patterns. The possibility of the real space Bravais lattice being rhombohedral can be ruled out on the following grounds: A rhombohedral cell related to fluorite will have its unique triad axis aligned with the

$\langle 111 \rangle_f$ axis since trigonal structures related to fluorite are not known to be oriented otherwise. As in the case of RhI it will have at the most 8 different orientation variants giving rise to $8 \times 2 = 16$ reflections for {100} type planes in the primitive reciprocal lattice cell. However, since this structure has triad symmetry one will expect to see 48 reflections arising from equivalent planes. Therefore there will be a total of 96 reflections in the BCC reciprocal lattice cell as in the case of the most general triclinic cell. However, in the case of the rhombohedral microdomain, calculations showed that strong reflections do occur in the $\langle 111 \rangle_f$ diffraction pattern corresponding to $\bar{1}\bar{1}\bar{1}$ type reflections; in the experimental urania-yttria $\langle 111 \rangle_f$ pattern this is not observed and so this possibility can be ruled out. An orthorhombic microdomain can also be dismissed because there are in general 6 ways of arranging such a domain in a cubic matrix which will give rise to 24 equivalent spots in the *Im*3*m* space group. It can therefore be concluded that the most likely symmetry of the real space Bravais lattice present in this case is monoclinic. The problem of solving the microdomain structure ab initio in this system is difficult. The approach suggested above is a tentative attempt to make some progress. To go beyond the ideas put forward would require far more extensive analysis.

The model for urania-ceria on the other hand envisages microdomains of a known structure—that of pyrochlore—where each microdomain has one set of $\{111\}_f$ planes that are more strongly ordered than others. These domains are approximately rod shaped, where the rod axis is aligned perpendicular to the strongly ordered $\{111\}_f$ planes and the rod diameter is approximately half the rod axis.

Acknowledgments

The authors thank Dr. Henry Rossell for helpful correspondence and for providing a copy of his computer program and Dr. Badwal for specimens of urania-yttria and Dr. Murray for specimens of urania-ceria. M.C.P. thanks the S.E.R.C. for financial support.

References

1. P. Herrero, P. Garcia-Chain, and R. M. Rojas, *J. Solid State Chem.* **87,** 331 (1990).
2. U. Wichmann, U. Berndt, and C. Keller, *Rev. Chim. Miner.* **14,** 105 (1977).
3. H. J. Rossell, *J. Solid State Chem.* **19,** 103 (1976).
4. S. F. Bartram, E. F. Juenke, and E. A. Aitken, *J. Am. Ceram. Soc.* **47,** 171 (1964).
5. S. F. Bartram and E. S. Fitzsimmons, *J. Nucl. Mater.* **35,** 126 (1970).
6. J. B. Ainscough and I. F. Ferguson, *J. Inorg. Nucl. Chem.* **36,** 193 (1974).
7. T. L. Markin, R. S. Street, and E. C. Crouch, *J. Inorg. Nucl. Chem.* **32,** 59 (1970).
8. M. C. Pienkowski, M. L. Jenkins, J. L. Hutchison, and P. T. Moseley, *Mater. Res. Soc. Symp. Proc.* **121,** 623 (1988).
9. J. G. Allpress and H. J. Rossell, *J. Solid State Chem.* **15,** 68 (1975).
10. B. Hudson and P. T. Moseley, *J. Solid State Chem.* **19,** 383 (1976).
11. S.P.S. Badwal and D. J. M. Bevan, *J. Mater. Sci.* **14,** 2353 (1979).
12. E. A. Aitken and R. A. Joseph, *J. Phys. Chem.,* 1090 (1966).
13. A. D. Murray, C. R. A. Catlow, and B. E. F. Fender, *J. Chem. Soc., Faraday Trans. 2* **83,** 1113 (1987).
14. H. Matzke, *J. Chem. Soc., Faraday Trans. 2* **83,** 1121 (1987).
15. A. W. Hull, *Phys. Rev.* **9,** 84, 564 (1917); **10,** 661, (1917).
16. P. Debye and P. Scherrer, *Phys. Z.* **17,** 277 (1916); **18,** 291, (1917).
17. M. U. Cohen, *Rev. Sci. Instrum.* **6,** 68 (1935).
18. M. G. Paton and E. N. Masten, *Acta Crystallogr.* **19,** 307 (1965).
19. G. V. Tendeloo and S. Amelinckx, *Scr. Metall.* **20,** 335 (1986).
20. J. Billingham, P. S. Bell, and M. H. Lewis, *Acta Crystallogr., Sect. A* **28,** 602 (1972).
21. J. R. Castles, J. M. Cowley, and A. E. C. Spargo, *Acta Crystallogr., Sect. A* **27,** 376 (1971).
22. M. Sauvage and E. Parthe, *Acta Crystallogr., Sect A* **28,** 607 (1972).
23. T. L. Markin, R. S. Street, and E. C. Crouch, *J. Inorg. Nucl. Chem.* **32,** 77 (1970).
24. D. J. Smith, W. O. Saxton, M. A. O'Keefe, G. J. Wood, and W. M. Stobbs. *Ultramicroscopy* **11,** 263 (1983).
25. M. P. Herrero and R. M. Rojas, *J. Solid State Chem.* **73,** 536 (1988).

26. R. L. MARTIN, *J. Chem. Soc. Dalton Trans.* 1335 (1974).
27. O. MULLER AND R. ROY, *Mater. Res. Bull.* **4,** 349 (1969).
28. G. I. TYUSHEVSKAYA, N. S. AFONSKII, AND V. I. SPITSYN, *Dokl. Akad. Nauk SSR* **170,** 859 (1966).
29. R. D. SHANNON AND C. T. PREWITT, *Acta Crystallogr., Sect. B* **25,** 925 (1969).
30. F. BRISSE AND O. KNOP, *Can. J. Chem.* **46,** 859 (1968).
31. R. D. SHANNON AND A. W. SLEIGHT, *Inorg. Chem.* **7,** 1649 (1968).
32. K. LONSDALE (Ed.), "International Tables for X-Ray Crystallography," Vol. I, Kynoch Press, Birmingham (1963).